The cosmic ray energy spectrum measured with the Pierre Auger Observatory

Francesco Fenu [a,1,*], for the Pierre Auger Collaboration [b,2]

[a] Karlsruhe Institute of Technology, Hermann von Helmholtz Platz 1, 76344 Eggenstein-Leopoldshafen, Germany
[b] Observatorio Pierre Auger, Av. San Martín Norte 304, 5613 Malargüe, Argentina

Abstract

In this contribution, we present the latest updates on the energy spectrum characterization obtained with data from the Pierre Auger Observatory. We present the measurement of the spectrum from 6×10^{15} eV up to above 10^{20} eV, obtained by combining five different methods. The exposure of over 80,000 km^2 sr yr has been accumulated above the ankle region, making this the best estimate of the spectrum ever achieved in this energy range. The wide zenith angle range covered by the Pierre Auger Observatory and the enormous exposure also allow us to measure the spectrum in different regions of the sky. After a description of the techniques used to reconstruct the spectrum, the spectral features will be presented, and the astrophysical implications of the spectral shape will be briefly discussed.

Keywords: Cosmic rays; Energy spectrum; Pierre Auger Observatory

1. Introduction

The Pierre Auger Observatory (Aab et al., 2015c) is the largest cosmic ray observatory ever built. It is located in Argentina, near the town of Malargüe, at an altitude of 1400 m and covers an area of 3000 km^2. It consists of a Surface Detector (SD), an array of 1600 stations deployed on a triangular grid of 1500 m spacing (referred to as SD1500), designed to detect the secondary particles of Extensive Air Showers (EAS) on the ground. A Fluorescence Detector (FD), consisting of 24 telescopes in four buildings (Abraham et al., 2010a), overlooks the SD, covering the elevation range 2 to 32°, to detect the longitudinal development of the shower in the atmosphere through the EAS fluorescence emission. Each SD station consists of a tank of 12 T of water, monitored by three PMTs of nine inches diameter, within which the secondary particles emit Cherenkov light. With the SD signal, detected with a nearly 100% duty cycle, it is possible to reconstruct the geometry of the shower and the distribution of the secondary particles on the ground. With such a distribution it is then possible to reconstruct an energy estimator, a parameter proportional to the energy for each of the SD events. The longitudinal profile is instead measured with the FD, allowing us to measure the energy almost calorimetrically. Such a measurement is possible only approximately 13% of the time after having excluded day time and bad weather conditions.

The Pierre Auger Observatory is based on the so-called hybrid design, in which the bulk of the events is detected with the SD, while a sub-sample of events detected by both SD and FD (the Hybrid events) is used to calibrate the energy estimator of the SD. The SD energy is therefore

* Corresponding author.
E-mail addresses: francesco.fenu@gmail.com, spokespersons@auger.org.
[1] Now at Agenzia Spaziale Italiana, Via del Politecnico, 00133 Rome, Italy.
[2]

Table 1
Main data set parameters as presented in Novotny et al. (2021). The first three data sets are based on SD data. Hybrid and Chrenkov are based on FD data.

	SD1500 $< 60°$ (SD)	SD1500 $> 60°$ (SD)	SD750 (SD)	Hybrid (FD)	Cherenkov (FD)
Exposure [km^2 sr yr]	60400	17500	105	2600 @10^{19} eV	2.2 @10^{17} eV
Number of events	215030	24209	545090	14675	123159
Data taking period	01/2004–08/2018	01/2004–08/2018	01/2014–08/2018	01/2007–12/2017	06/2012–12/2017
Zenith angle range [°]	0–60	60–80	0–40	0–60	0–85
Energy threshold [eV]	$10^{18.4}$	$10^{18.6}$	10^{17}	10^{18}	$10^{15.8}$

estimated with minimal reliance on simulations, which are based on models extrapolated from energies in the accelerator domain[3], and therefore affected by large uncertainties.

The SD is enhanced with a low energy extension, the SD750, where 64 stations are deployed over an area of 24 km^2 with a 750 m spacing. Thanks to such an extension, the full efficiency range of the SD is lowered to 10^{17} eV from $10^{18.4}$ eV of the SD1500. The FD is also extended to the lower energies with 3 additional telescopes, the High Elevation Auger Telescopes (HEAT). Such telescopes point to a higher elevation (from 30 to 58°) and detect events dominated by the Cherenkov emission in the atmosphere, lowering the energy threshold of the FD from 10^{18} to $10^{15.8}$ eV.

Five data sets are used by the collaboration to reconstruct the spectrum over several orders of magnitude in energy and over a large zenith angle range: the SD1500 under 60° zenith angle, the SD1500 above 60°, the SD750, the Hybrid and the Cherenkov data set. The most important parameters of these data sets are shown in Table 1. In the following, we present the status of the energy spectrum of the Pierre Auger Observatory and give a brief description of the techniques used. We present the combined spectrum from $10^{15.8}$ eV up to above 10^{20} eV.

2. The Surface Detector spectra

Thanks to the nearly 100% duty cycle of the SD and its enormous area, a gigantic exposure (now $\sim$ 80,000 km^2 sr yr) can be collected. The highest energy region of the spectrum is therefore measured with unrivaled precision. The most recent updates on the spectrum above 10^{17} eV can be found in Aab et al. (2020b), Abreu et al. (2021) for the SD1500 and SD750 spectra respectively and Aab et al. (2015a), Novotny et al. (2021) for the SD1500 spectrum above 60°.

Only events in which the station with the highest signal is surrounded by six active stations are selected. The verification of this condition guarantees an optimal sampling of the event since it excludes the borders of the array and non-active regions. This selection criterion also ensures that the shower core is inside a 1.95 km^2 hexagon centered on the most active station. The total exposure is calculated by integrating the aperture of the selected hexagons (4.59 km^2 sr) over time. The exposure can be therefore calculated in a geometrical way, without the aid of Monte Carlo (Abraham et al., 2010c), independent of the energy and with uncertainty at the level of $\sim 3\%$.

The signal of the single stations is calibrated with the natural flux of cosmic ray muons. This source, common to all the stations, very uniform and stable in time is used to define the so called Vertical Equivalent Muon (VEM), the signal of a vertical muon crossing the station. In this way, it is possible to obtain a relative calibration of the signal amplitude between the stations (Bertou et al., 2006).

A fit of the timing and amplitude of the signal of the single stations is used to determine the impact point and the shower direction for each event (Aab et al., 2020c) with a resolution of 1° and 50 m, respectively.

The signal amplitude as a function of the position on the ground is then fit to obtain an energy estimator. Each data set has a specific energy estimator: $S(1000), S(450)$ and N_{19} for the SD1500, SD750 and the SD1500 above 60° zenith angle, respectively. The $S(1000)$ and $S(450)$ parameters are obtained by fitting a Lateral Distribution Function (LDF) to the signal amplitude as a function of the distance from the shower axis. The values of the signal amplitude at 1000 or 450 m from the shower axis are the ones proven to be least affected by uncertainties. The events above 60° need a dedicated treatment as are affected by a large attenuation and they are dominated by muons on the ground (Aab et al., 2014b). The effect of the geomagnetic field destroys the circular symmetry of the LDF for such kind of events. The identification of a single radial distance for the definition of the energy estimator is therefore not possible anymore. In this case, the estimator N_{19} is rather the scaling factor needed to fit the bi-dimensional MC distribution of muons on the ground ($\rho_{\mu,19}$ of a proton shower at 10^{19} eV) to data

$$\rho_\mu(\vec{r}) \quad N_{19}\rho_{\mu,19}(\vec{r},\Theta,\Phi), \tag{1}$$

where Θ and Φ are the zenith and azimuth angles of the shower arrival direction, respectively, and $\vec{r}$ is the position within the observatory where we evaluate the signal.

At the Auger atmospheric depth ($\sim$875 g/cm^2), showers have already passed the maximum and are in the attenuation phase. Showers with larger zenith angles are more attenuated than vertical ones because of the larger amount of matter they have to traverse. Therefore, the energy

[3] In the center-of-mass reference system for proton-proton collision, cosmic rays reach $\sim$ 400 TeV, compared to 14 TeV of the LHC.

estimators have a dependence on the zenith angle. The energy estimators $S(1000)$ and $S(450)$ are then corrected with a data-driven method: the Constant Intensity Cut (CIC) method (Hersil, 1961). This method is based on two assumptions: the isotropy of the arrival direction of cosmic rays and the full efficiency of the array above a certain energy threshold. Under these assumptions, generally valid above the threshold, the intensity (i.e. the event rate per steradian) can be used as a proxy for the energy. The value of $S(1000)$ and $S(450)$ as a function of the zenith angle, measured at a constant intensity, can be therefore used to determine the attenuation in the atmosphere. In Aab et al. (2020b), Abreu et al. (2021) the attenuation has been estimated for the first time at different energies (see Fig. 1)) to account for the evolving mass composition and the energy-dependent muonic fraction. After the correction of the attenuation, we obtain new energy estimators as they would appear at fixed zenith angles, S_{38}, at 38°, and S_{35}, at 35°, for the SD1500 and the SD750, respectively.

The shower size estimator is then converted into energy with a subset of the FD events that have also triggered the SD. Selection criteria are applied to guarantee a precise estimation of $E_{\rm FD}$. Fiducial cuts are also applied to minimize mass-dependent biases in the exposure and, therefore biases on the energy estimator distribution. The correlation between the FD energy and the energy estimator is shown in Fig. 2 and is fit with the function

$$E_{\rm FD} \quad A\widehat{S}^{B}, \tag{2}$$

where $\widehat{S}$ is the energy estimator (S_{38}, S_{35} or N_{19}). The A and B parameters are then used to convert the energy estimator into an energy for all the SD events ($E_{\rm SD}$). The energy scale is known at the level of 14%, with the largest uncertainties coming from the detector calibration 9.9%, from the knowledge of the atmosphere 6.2%, and from the reconstruction technique uncertainty $\sim$ 6%. A detailed overview

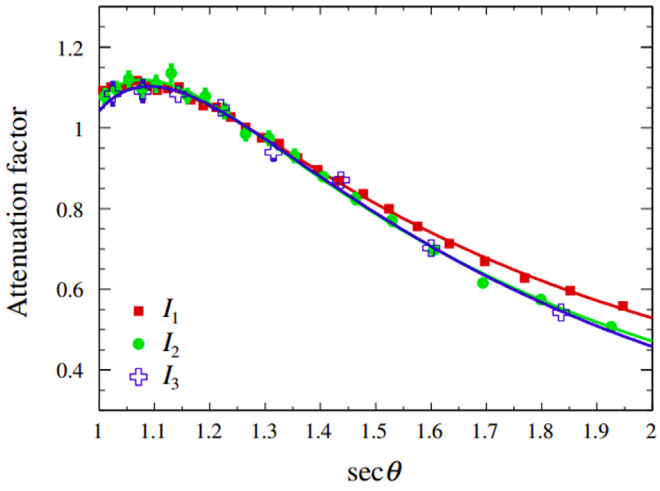

Fig. 1. The attenuation factor as calculated in Aab et al. (2020b). Three different intensities roughly corresponding to 3×10^{18} eV, 8×10^{18} eV and 2×10^{19} eV are shown here.

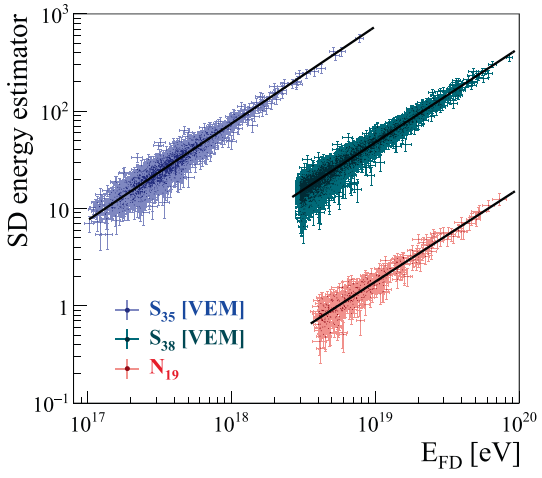

Fig. 2. The correlation between the FD energy and the energy estimators with the best fit function in black (Novotny et al., 2021).

of all the sources of uncertainties is given in Verzi (2013). As described in Aab et al. (2020b), the resolution for the SD1500 is estimated from hybrid events by calculating the ratio $\frac{E_{\rm SD}}{E_{\rm FD}}$. Thanks to the lower energy threshold of the hybrid data set with respect to the SD, it is also possible to estimate the sub-threshold bias and the SD efficiency by comparing the two data sets. For the SD750 spectrum, given the low energy threshold, the bias must be instead calculated with simulations, while the efficiency is calculated from a data-driven parameterization of the Lateral Trigger Probability (LTP), the probability that a shower of a certain energy will produce a station level trigger as a function of the distance from the core (see Abreu et al., 2021; Abreu et al., 2011b for more details).

The so-called raw spectrum is reconstructed as

$$J_i^{\rm raw} \quad \frac{N_i}{\mathcal{E}\Delta E_i}, \tag{3}$$

where $J_i^{\rm raw}$ is the raw spectrum in the i^{th} bin, N_i is the event rate, $\mathcal{E}$ the exposure, and ΔE_i is the width of the energy bin.

The Collaboration adopts a forward-folding technique to correct for detector effects. In this approach, a sequence of power laws is assumed

$$J(E;\mathbf{s}) \quad J_0\left(\frac{E}{E_0}\right)^{-\gamma_1}\prod_{i=1}^{3}\left[1+\left(\frac{E}{E_{ij}}\right)^{\frac{1}{\omega_{ij}}}\right]^{(\gamma_i-\gamma_j)\omega_{ij}}, \tag{4}$$

where $J(E)$ is the differential flux as a function of the energy, J_0 is the normalization at E_0 $10^{18.5}$ eV, γ_i is the spectral index, $E_{i,j}$ is the transition between two power law regions and j $i+1$. The tunable transition widths ω_{12}, ω_{23} and ω_{34} are set to 0.05. Such value corresponds to a transition within one logarithmic bin of 0.1 width. No indication of wider transitions is found in the data.

Detector effects are accounted for by means of a forward-folding procedure. The spectral parameters are fit to data, after the inclusion of the smearing, with a Poissonian likelihood maximization. The ratio between the true

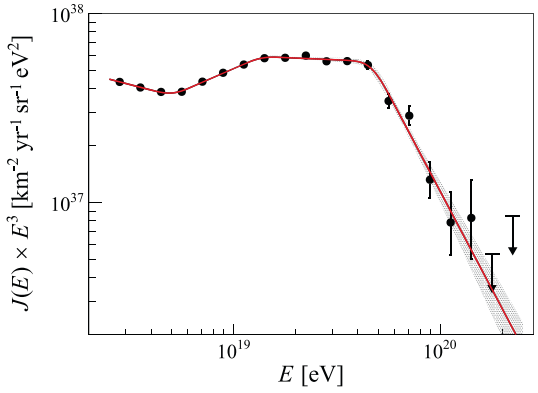

Fig. 3. The SD1500 unfolded spectrum with the fitting function. The last two points are 90% CL Feldman Cousins limits. Plot from Aab et al. (2020b).

and folded rate is used as a correction factor on the raw spectrum to give an estimate of the unfolded spectrum $J(E)$. We show the unfolded SD1500 spectrum in Fig. 3, together with the fitting function (Aab et al., 2020b). Other important results include the detection of a new feature beside the ankle, at 5×10^{18} eV, and the suppression, at 5×10^{19} eV, namely the instep at 10^{19} eV. No significant dependence on declination has been found in the spectrum. Moreover, the SD750 spectrum allows us to measure the full range from 10^{17} eV to the highest energies. In particular, the range from the second knee to the ankle is crucial to understand the transition from galactic to extragalactic cosmic rays. The SD1500 spectrum above 60° increases the exposure of the SD1500 spectrum by roughly 30% and extends the sky coverage of Auger toward the Northern sky. This feature is of extreme importance both from the astrophysical point of view and also for future comparisons with the Telescope Array observatory, the largest observatory in the northern hemisphere (Kawai et al., 2008). All the SD spectra are shown in Fig. 4 (Novotny et al., 2021).

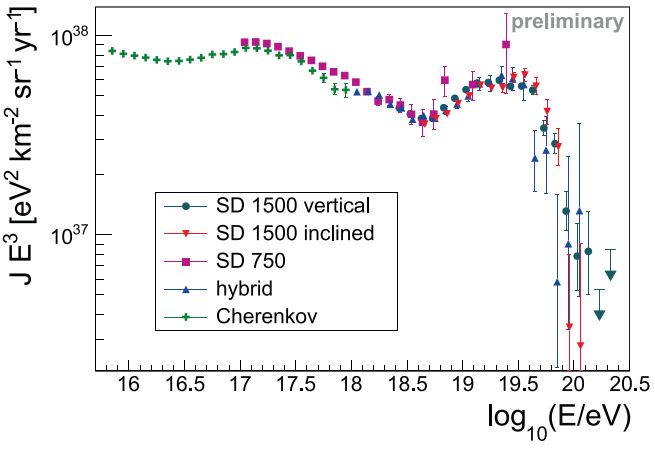

Fig. 4. The five Pierre Auger spectra as presented in Novotny et al. (2021).

3. The Fluorescence Detector spectra

The FD of the Pierre Auger Observatory is used to produce two further estimates of the spectrum: the hybrid spectrum and the Cherenkov spectrum. The FD event is reconstructed with a fit on the timing and the arrival direction of the fluorescence photons, where a test geometry prediction is fit to data. The direction pointed by the illuminated pixels in the sky is used to identify the so-called shower-detector plane, the plane where we both have the detector and the shower axis. The arrival time of the photons is fit to determine the direction of the shower in this plane (Abraham et al., 2010b). Both spectra generally rely on events detected in monocular mode, although a smaller fraction of high-quality events is detected from multiple sites, and can therefore be also reconstructed in stereo mode. The apparent speed of the event on the focal surface depends on both the distance and direction of the event with respect to the telescope. The correlation of such parameters has to be removed with external information, either from the SD timing (as it will be shown for the hybrid spectrum) or from constraints on the longitudinal profile (as for the Cherenkov spectrum). The profile of the event is reconstructed, accounting for the detector efficiency, for the atmospheric attenuation and for the fluorescence yield (Ave et al., 2013). The energy deposition as a function of the traversed amount of matter is then calculated and fit with a Gaisser-Hillas (GH) function (Aab et al., 2019b). The integral of the function gives the calorimetric energy ($E_{\rm cal}$), the total energy deposited in the atmosphere. To obtain the FD energy, it is necessary to correct for the so-called invisible energy, the energy carried to the ground by muons and neutrinos. Such particles do not contribute to the energy deposition in the atmosphere and would therefore result in an energy underestimation if not properly accounted for. The Collaboration uses a data-driven method for the calculation of this missing energy (Aab et al., 2019a), in this way, avoiding the use of models, known to fail to describe the muon data at such energies (Aab et al., 2015b).

Both for the hybrid and for the Cherenkov spectrum, the exposure must be calculated with a Monte Carlo (Abreu et al., 2011a). A large number of events is simulated uniformly in core position and zenith angle. The status of the observatory at the exact acquisition time and the atmospheric conditions are taken into account in the simulation (for details, see Abreu et al., 2011a). The exposure of both spectra strongly depends on the energy. Further cuts have to be applied to reduce the dependence of the exposure on the mass. Indeed, light primaries typically give origin to showers that develop deeper in the atmosphere compared to heavier ones, and a selection bias is to be expected at the edges of the field of view. The so-called fiducial field of view cut is implemented on the maximal and minimal depth of the shower maximum, thus reducing the primary

mass dependence of the exposure to $\sim 8\%$ at 10^{18} eV and $\sim 1\%$ above 10^{19} eV(Aab et al., 2014a).

The hybrid spectrum (Settimo, 2012; Novotny et al., 2021) is based on events that trigger on the FD and with at least one SD station triggering on the ground. The events are selected to guarantee an accurate reconstruction of the shower energy and to minimize the biases in a similar way as done for the calibration. Furthermore, only events whose maximum is inside the field of view are accepted. Showers pointing toward the telescopes are excluded to avoid direct Cherenkov contamination. Selected showers have a residual back-scattered Cherenkov contamination of the order of 10–20%, which can be modeled and corrected.

Further cuts are applied to the atmospheric conditions: only events for which the aerosol content is known and for which the cloud coverage is limited to less than 25% are selected. Cuts are applied on the maximal distance of the shower from the detector to reduce the effect of the 14% uncertainty in the energy scale mentioned above on the trigger probability. Only events within a certain distance (depending on the energy but of the order of up to tens of km) from the detector are selected, to guarantee a stable exposure against a 14% energy shift. The spectrum is reconstructed in a similar way as described in Eq. 3 and covers the range from 10^{18} eV up to the highest energies (despite the much lower statistics than the SD spectra). This spectrum is shown again in Fig. 4.

The Cherenkov spectrum is the low-energy extension of the Auger spectrum down to 6×10^{15} eV (Novotny et al., 2021). Such events are FD events dominated by the Cherenkov emission and have no SD counterpart. The data set is built with the previously mentioned HEAT telescopes, which cover the high-elevation range. The detector is designed to detect events directly pointing to the telescopes that are therefore dominated by the Cherenkov emission. The geometry of the shower is reconstructed with the so-called Profile Constrained Geometry Fit (PCGF) method (Abbasi et al., 2008). A scan of all the geometries compatible with the arrival times of the photons is performed and, for each trial, the GH profile is calculated. The geometry that gives the best fit of the shower profile is chosen.

The Cherenkov data set consists of two samples. The first, the so-called T3 events, is the sample with the fully triggered events. Such events are the ones that satisfy the full chain of FD trigger conditions. In the second group, we have the so-called minimum bias events, a sample consisting of the 10% of the events that do not satisfy the last step of the trigger chain (namely, only the T3 trigger). Such events are used as a further low-energy enhancement, improving the statistics at $\sim 10^{16}$ eV by a factor of around two.

Also, for the Cherenkov spectrum, cuts are applied to guarantee a proper reconstruction and to minimize the biases. We again require that the maximum of the shower is in the field of view and that $\chi^2 < 3$ for the fit of the deposit profile. We, moreover, apply the so-called field of view cuts to limit the mass dependence of the exposure. In this case, however, a cut on the minimum Cherenkov fraction (50%) is applied. Fiducial volume cuts to ensure the stability of the exposure with respect to the energy scale uncertainty are also applied. For this purpose, a cut on the core distance together with a cut on the viewing angle (the angle between the line of sight of the observer and the shower axis) is applied.

A forward-folding technique is applied in this case, too, whereas resolution, bias and exposure are obtained through Monte Carlo. The unfolded Cherenkov spectrum is shown in Fig. 4. The Cherenkov spectrum is the only spectrum capable, at the moment, of covering the entire second knee and the low-energy ankle regions. The difference in normalization visible in the figure is of the order of $\sim$7%, within the systematic uncertainty on the Cherenkov spectrum exposure ($\sim$12%).

4. The combined spectrum

The combination technique was developed in Abreu et al. (2021) to combine the SD750 and SD1500 spectra and further extended to all the five spectra in Novotny et al. (2021). All the five spectra are combined through a forward-folding approach. For each of them, we estimated a migration matrix describing the effect of the detector on the spectral shape. All the uncorrelated systematic uncertainties between the methods have also been estimated. Such uncertainties are not common to the data sets and allow for changes in the position of the spectra relative to each other. The assumed input function has the same shape as in Eq. 4 but with six power laws and five tunable breaks. The fit consists of a single Likelihood maximization based on a Poissonian component, where the expected folded rate is compared to data for each of the single data sets. To each of the five data sets, a shift in exposure and energy is applied to account for possible systematic differences between the spectra. A Gaussian penalization is included in the Likelihood to avoid arbitrary shifts in the energy and exposure. Such penalization decreases the Likelihood for each condition in which the energy or exposure shifts are larger than the expected uncorrelated systematics. In this way, it is guaranteed that the shifts we apply are not unphysical and are generally within the systematic uncertainties. A scan of the energy and exposure shifts is applied, and the set of parameters that best describes data is chosen. As can also be seen in Fig. 4, all the spectra are generally in good agreement. The exposure of the Cherenkov spectrum must be decreased by 7% to obtain the best fit with a single input function, thus increasing its normalization. At the same time, a combination of exposure and energy shifts will increase the normalization of the SD1500 spectrum above 60° by 5%. Finally, the SD750 spectrum normalization has to be shifted down by 2%. Such shifts are well within the systematic uncertainties, with some degree of tension only for the SD1500 above 60°.

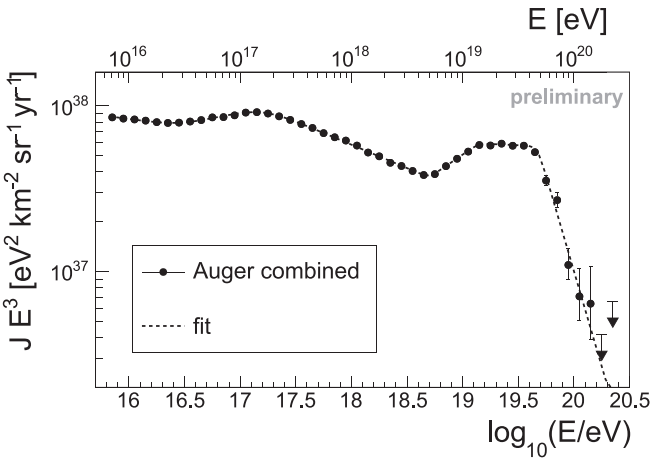

Fig. 5. The Pierre Auger combined energy spectrum as presented in Novotny et al. (2021).

Table 2
Spectral parameters of the Pierre Auger energy spectrum as presented in Novotny et al. (2021).

$J_0 = (8.34 \pm 0.04 \pm 3.40) \times 10^{11}$ km^{-2} sr^{-1} yr^{-1} eV^{-1}	$\gamma_0 = 3.09 \pm 0.01 \pm 0.10$
$E_{01} = (2.8 \pm 0.3 \pm 0.4) \times 10^{16}$ eV	$\gamma_1 = 2.85 \pm 0.01 \pm 0.05$
$E_{12} = (1.58 \pm 0.05 \pm 0.2) \times 10^{17}$ eV	$\gamma_2 = 3.283 \pm 0.002 \pm 0.10$
$E_{23} = (5.0 \pm 0.1 \pm 0.8) \times 10^{18}$ eV	$\gamma_3 = 2.54 \pm 0.03 \pm 0.05$
$E_{34} = (1.4 \pm 0.1 \pm 0.2) \times 10^{19}$ eV	$\gamma_4 = 3.03 \pm 0.05 \pm 0.10$
$E_{45} = (4.7 \pm 0.3 \pm 0.6) \times 10^{19}$ eV	$\gamma_5 = 5.3 \pm 0.3 \pm 0.1$

The combined Auger spectrum is shown in Fig. 5 with the fitting function. The resulting spectral parameters are presented in Table 2. The transition width parameters are fixed to ω_{01} ω_{12} 0.25 and ω_{23} ω_{34} ω_{45} 0.05. Further studies are ongoing to measure the actual width of the low-energy ankle (at $\sim 2.8 \times 10^{16}$ eV) and of the second knee (at $\sim 10^{17}$ eV) while, for the higher energies transitions, the same arguments as discussed for Eq. 4 are valid.

5. Conclusions

The combined spectrum covers almost five orders of magnitude in energy, the entire range measured by ground-based detectors. The spectrum can be well described by a sequence of power laws with several changes in steepness: the low-energy ankle at $\sim 2.8 \times 10^{16}$ eV, the second knee at $\sim 1.58 \times 10^{17}$ eV, the ankle at $\sim 5 \times 10^{18}$ eV, the instep at $\sim 1.4 \times 10^{19}$ eV and the suppression at $\sim 5 \times 10^{19}$ eV. The spectral features bear information on the production mechanisms, but the combination of additional external information is needed to study the cosmic ray origin.

From the large-scale anisotropy measured above 8×10^{18} eV (Aab et al., 2017b), it is possible to infer the extragalactic nature of the sources. Indications of possible sources come from correlation studies with potential classes of sources (Aab et al., 2018) with Starburst Galaxies as the sources that give the most significant deviation from isotropy. Furthermore, composition studies indicate a progressively heavier mass toward the highest energies (Yushkov, 2019).

A combined fit of spectral shape and composition is then used to interpret the shape of the spectrum (Aab et al., 2017a). Such studies favor a scenario in which cosmic rays are accelerated in magnetized sources where the maximal energy is proportional to the charge Z. In this picture, the average mass increases with energy given the lower magnetic rigidity of heavier primaries. It is, therefore, easier to confine such particles in the acceleration environments, and such primaries reach higher energies. In this scenario, the suppression is to be regarded as the mixed effect of the maximal acceleration of heavy cosmic rays in the source and propagation effects. The instep is instead resulting from the interplay between a helium-dominated flux under 10^{19} eV to a carbon–nitrogen-oxygen-dominated flux above such energy (Aab et al., 2020a). Moreover, the highest-energy region of the spectrum can be well explained with extragalactic sources, while to explain the ankle feature, additional galactic components have to be considered (Guido et al., 2021).

The upgrade of the Pierre Auger Observatory (Aab et al., 2016), in the phase of completion, will add further observables to the measurement of the spectrum. A scintillator is being installed on each station to enhance the mass sensitivity of the SD. A small diameter PMT (1 inch) will extend the dynamic range of the observatory. A new electronics will allow the sampling of the SD signal with 8 ns instead of the present 25 ns resolution. The installation of a radio antenna on each station will also allow us to measure the radio emission of the shower in the atmosphere. All such new observables will be very valuable in the reconstruction of the spectrum. With such new data, it will be possible to reconstruct spectra in mass groups, adding valuable information for the production mechanism studies. With an extended dynamic range, we will be able to test saturation effects at the highest energies and better investigate the suppression region. The antennas will also improve the knowledge of the energy scale of the observatory by offering a complementary technique to measure the calorimetric energy.

Declaration of Competing Interest

The authors declare that they have no known competing financial interests or personal relationships that could have appeared to influence the work reported in this paper.

References

Aab, A. et al., 2014a. Depth of maximum of air-shower profiles at the Pierre Auger Observatory. I. measurements at energies above $10^{17.8}$ eV. Phys. Rev. D 90.

Aab, A. et al., 2014b. Reconstruction of inclined air showers detected with the Pierre Auger Observatory. J. Cosmol. Astropart. Phys. 2014, 019–019.

Aab, A. et al., 2015a. Measurement of the cosmic ray spectrum above 4×10^{18} eV using inclined events detected with the Pierre Auger Observatory. J. Cosmol. Astropart. Phys. 2015, 049–049.
Aab, A. et al., 2015b. Muons in air showers at the Pierre Auger Observatory: Mean number in highly inclined events. Phys. Rev. D 91.
Aab, A. et al., 2015c. The Pierre Auger Cosmic Ray Observatory. Nucl. Instrum. Methods Phys. Res., Sect. A 798, 172–213.
Aab, A. et al., 2016. The Pierre Auger Observatory Upgrade - preliminary design report.
Aab, A. et al., 2017a. Combined fit of spectrum and composition data as measured by the Pierre Auger Observatory. J. Cosmol. Astropart. Phys. 2017, 038–038.
Aab, A. et al., 2017b. Observation of a large-scale anisotropy in the arrival directions of cosmic rays above 8×10^{18} eV. Science 357, 1266–1270.
Aab, A. et al., 2018. An indication of anisotropy in arrival directions of ultra-high-energy cosmic rays through comparison to the flux pattern of extragalactic gamma-ray sources. Astrophys. J. 853, L29.
Aab, A. et al., 2019a. Data-driven estimation of the invisible energy of cosmic ray showers with the Pierre Auger Observatory. Phys. Rev. D 100.
Aab, A. et al., 2019b. Measurement of the average shape of longitudinal profiles of cosmic-ray air showers at the Pierre Auger Observatory. J. Cosmol. Astropart. Phys. 2019, 018–018.
Aab, A. et al., 2020a. Features of the energy spectrum of cosmic rays above 2.5×10^{18} eV using the Pierre Auger Observatory. Phys. Rev. Lett. 125.
Aab, A. et al., 2020b. Measurement of the cosmic-ray energy spectrum above 2.5×10^{18} eV using the Pierre Auger Observatory. Phys. Rev. D 102.
Aab, A. et al., 2020c. Reconstruction of events recorded with the surface detector of the Pierre Auger Observatory. J. Instrum. 15, P10021–P10021.
Abbasi, R.U. et al., 2008. First observation of the Greisen-Zatsepin-Kuzmin suppression. Phys. Rev. Lett. 100.
Abraham, J. et al., 2010a. The fluorescence detector of the Pierre Auger Observatory. Nucl. Instrum. Methods Phys. Res., Sect. A 620, 227–251.
Abraham, J. et al., 2010b. The fluorescence detector of the Pierre Auger Observatory. Nucl. Instrum. Methods Phys. Res., Sect. A 620, 227–251.
Abraham, J. et al., 2010c. Trigger and aperture of the surface detector array of the Pierre Auger Observatory. Nucl. Instrum. Methods Phys. Res., Sect. A 613, 29–39.
Abreu, P. et al., 2011a. The exposure of the hybrid detector of the Pierre Auger Observatory. Astropart. Phys. 34, 368–381.
Abreu, P. et al., 2011b. The lateral trigger probability function for the ultra-high energy cosmic ray showers detected by the Pierre Auger Observatory. Astropart. Phys. 35, 266–276.
Abreu, P. et al., 2021. The energy spectrum of cosmic rays beyond the turn-down around 10^{17} eV as measured with the surface detector of the Pierre Auger Observatory. The. Eur. Phys. J. C 81.
Ave, M. et al., 2013. Precise measurement of the absolute fluorescence yield of the 337nm band in atmospheric gases. Astropart. Phys. 42, 90–102.
Bertou, X. et al., 2006. Calibration of the surface array of the Pierre Auger Observatory. Nucl. Instrum. Methods Phys. Res., Sect. A 568, 839–846.
Guido, E. et al., 2021. Combined fit of the energy spctrum and mass compostion across the ankle with the data measured at the Pierre Auger Observatory. PoS, ICRC2021, 311
Hersil, J. et al., 1961. Phys. Rev. D 6.
Kawai, H. et al., 2008. Telescope Array experiment. Nucl. Phys. B - Proc. Suppl. 175–176, 221–226. Proceedings of the XIV International Symposium on Very High Energy Cosmic Ray Interactions.
Novotny, V. et al., 2021. Energy spectrum of cosmic rays measured using the Pierre Auger Observatory. PoS, ICRC2021, 324.
Settimo, M., 2012. Measurement of the cosmic ray energy spectrum using hybrid events of the Pierre Auger Observatory. Eur. Phys. J. Plus 127.
Verzi, V., 2013. The Energy Scale of the Pierre Auger Observatory. In: 33rd International Cosmic Ray Conference, p. 0928.
Yushkov, A., 2019. Mass composition of cosmc rays with energies above $10^{17.2}$ eV from the hybrid data of the Pierre Auger Observatory. PoS, ICRC2019, 482.